Brain white matter morphological structure correlation with its optical properties estimated from optical coherence tomography (OCT) data

ALEXANDER A. MOISEEV,[1] KSENIA A. ACHKASOVA,[2,*] ⓘ ELENA B. KISELEVA,[2] ⓘ KONSTANTIN S. YASHIN,[2] ARSENIY L. POTAPOV,[2] ⓘ EVGENIA L. BEDERINA,[2] SERGEY S. KUZNETSOV,[3] EVGENY P. SHERSTNEV,[1] DMITRY V. SHABANOV,[1] GRIGORY V. GELIKONOV,[1] ⓘ YULIYA V. OSTROVSKAYA,[4] AND NATALIA D. GLADKOVA[2]

[1]*Institute of Applied Physics Russian Academy of Sciences, 603155, 46, Ulyanova str., Nizhny Novgorod, Russia*
[2]*Privolzhsky Research Medical University, 603950, 10/1, Minin and Pozharsky sq., Nizhny Novgorod, Russia*
[3]*N.A. Semashko Nizhny Novgorod Regional Clinical Hospital, 603093, 190, Rodionova str., Nizhny Novgorod, Russia*
[4]*Dentistry clinic "IQDent", 105120, 10, 2nd Syromyatnichesky Lane, Moscow, Russia*
*achkasova.k@bk.ru

Abstract: A pilot post-mortem study identifies a strong correlation between the attenuation coefficient estimated from the OCT data and some morphological features of the sample, namely the number of nuclei in the field of view of the histological image and the fiber structural parameter introduced in the study to quantify the difference in the myelinated fibers arrangements. The morphological features were identified from the histopathological images of the sample taken from the same locations as the OCT images and stained with the immunohistochemical (IHC) staining specific to the myelin. It was shown that the linear regression of the IHC quantitative characteristics allows adequate prediction of the attenuation coefficient of the sample. This discovery opens the opportunity for the usage of the OCT as a neuronavigation tool.

1. Introduction

The number of papers devoted to the study of the brain white matter (WM) using optical methods has been growing in recent years [1–4]. The necessity to understand the relationship between the optical properties of the WM and its morphological features (the arrangement of fibers, the number of cells) also arises, since optical methods claim to be intraoperative diagnostic techniques of some diseases associated with invasion or damage to the WM.

　WM forms up to 40% of brain tissue and has a multicomponent structure including different cell types (mostly glial) and extracellular matrix [5]. Its main structural unit is myelinated fiber consisting of neuronal axonal process covered with a myelin sheath, formed by oligodendrocyte process. It is known, that structural characteristics of WM are not identical throughout the brain, where the differences can be detected in fibers diameter and their packing density [6–10] as well as the size and density of the glial cells [11]. Some brain areas are formed by parallel densely packed fibers that form so-called pathways (or tracts); others contain more loosely located fibers due to the inclusion of neurons or a large amount of glia. Accordingly, the concentration of fibers and cell nuclei per volume unit in such areas will be different. In our opinion, it is important to take these morphological features into account when using optical methods, such as optical coherence tomography (OCT).

OCT is a promising method in brain imaging finding application in translational studies and clinical practice [12]. The number of studies [3,4,13,14] have shown that OCT has a potential for studying the WM morphological features and for clarifying the boundaries of the infiltrative brain tumors within surrounding WM. In particular, high resolution OCT provides contrast imaging of myelinated nerve fibers, thereby allowing visualization of the pathways in the brain [14]. The addition of polarization sensitivity makes the method more specific to the direction of the bundles of nerve fibers [15]. Moreover, it has demonstrated good cross-validation with diffusion tensor imaging (DTI) [16] that is currently used for preoperative planning in brain tumor surgery providing the information about the location and orientation of white matter tracts in relation to the tumor mass.

Application of OCT for detection of glial tumors growth margin is based on visual (qualitative) assessment of light attenuation profile in B-scans [17–19] and quantitative analysis (mostly by calculating the threshold values of attenuation coefficient) of OCT data [3,4,19–21]. Commonly, there is no emphasis on the location of the tumor in the brain, where the WM samples are obtained. At the same time, the tumor can be located both near vital tracts and at a distance from them. It seems to be important to take into account the structure of WM when determining the criteria for the differential diagnosis of normal WM and a tumor. In [22], the dependence of the attenuation coefficient on the degree of WM infiltration by tumor cells was shown; however, the work devoted to the detailed analysis of the optical properties of normal WM in different areas of the brain and evaluating the effect of its morphological features on the attenuation coefficient is scarce. At the same time, the development of OCT approaches to detailed in vivo visualization of white matter, is extremely important since it will solve a number of clinical and experimental problems. On the one hand, the possibility of obtaining real-time information about the structural characteristics of the white matter in the operating room will allow the neurosurgeon to specify the boundaries of tumor resection and prevent damage to healthy pathways. On the other hand, real-time visualization of white matter tracts will allow experimental studying the diseases that damage myelinated fibers, as well as developing new treatment strategies without the need for long-term histological analysis. However, despite the fact that OCT allows obtaining high-resolution images of white matter, the relationship between the nature of the received signal and the morphological features of the white matter remains unexplored nowadays, which is critical for further study of the optical properties of the pathways.

The most reliable way to identify the structure of the white matter is immunohistochemical study (IHC) of histological sections using antibodies to the structural proteins of the myelin sheath. Most often, antibodies to myelin basic protein (MBP) are used due to the fact that it is the main structural element of the myelin sheath [23,24]. Staining is performed with antibodies labeled with the chromogen diaminobenzidine (DAB), which is a substrate for horseradish peroxidase. During the study, antibodies bind to their corresponding antigens, and DAB polymerizes to form a light brown product, which allows the identification of myelinated fibers. Additional staining of cell nuclei with hematoxylin is performed allowing evaluation of the amount of cells, where oligodendrocytes are the most widespread ones. Thus, as a result of IHC analysis, it is possible to assess the arrangement of the different fibers, as well as the number of cellular elements, regardless their specificity. In general, IHC sections may be analyzed using manual or automated techniques to count the cells and fibers amount relatively to the entire study area [25,26]. In the present study the relation between the quantitative IHC parameters and the attenuation coefficient, estimated from the OCT data was established and the linear model able to predict attenuation coefficient based on the IHC quantitative parameters was introduced.

While it is widely believed that the major factor affecting the attenuation coefficient of the WM sample is the density of the myelinated fibers, the dataset collected in the present study suggests otherwise. The statistical analysis shows that the observed difference in the attenuation coefficient values are explained mostly by the number of nuclei, observed in the IHC images field-of-view

and by the parameter, introduced in the present study aimed to reflect the how uniformly the fibers are distributed across the IHC image. The lack of dependence of the attenuation coefficient on the fibers density, defined in the present study as a ratio of the area, occupied by the fibers in the IHC image to the area of the image, can be explained by the narrow range of the fiber density values in the collected dataset. Thus, the possibility still remains that the fiber density is the major factor, affecting the attenuation coefficient and just the peculiarities of the collected dataset do not allow to reflect this fact. However, the present study strongly suggests that the other morphological factors also influence the attenuation coefficient value and should be taken into account while analyzing the factors affecting the optical properties of the WM samples.

2.   Materials and methods

### 2.1.   Tissue samples and design of the study

The study was conducted on 6 post-mortem human brain specimens (3 right and 3 left hemispheres), obtained from patients aged from 58 to 69, whose death was not caused by intracranial pathology.

The regions of interest included different areas of white matter and fiber tracts, both superficial and deep-seated, with different arrangement of fibers and the number of cells. In total, 24 samples of white matter and fiber tracts were obtained from following brain areas: (1) cortical - U-shaped fibers (n = 6); (2) subcortical - long-range association fibers (n = 8); (3) corpus callosum (n = 4); (4) capsula interna (n = 3); (5) brainstem (n = 3) (Fig. 1). The surface of the samples under study varied from 0.5×1 cm to 0.7×1.5 cm.
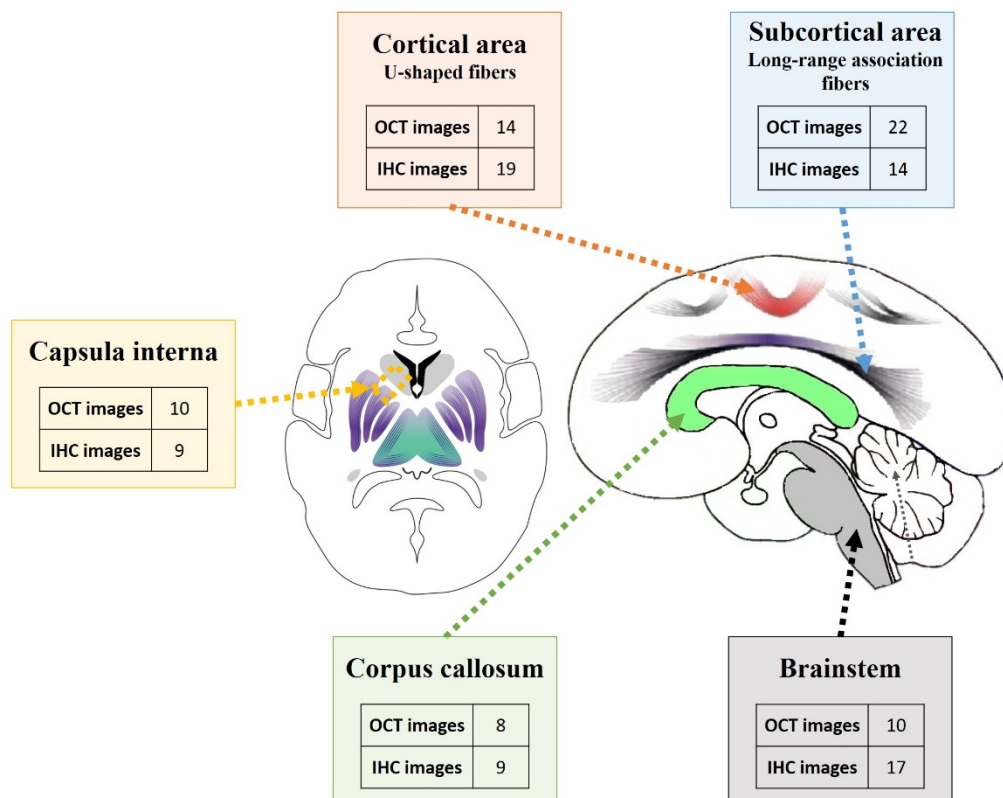
Fig. 1. The regions of interest where the white matter samples were collected and the amount of obtained OCT and IHC images.

On each sample, the area designated for the OCT study was marked with a surgical suture. After obtaining OCT images, all samples were fixed in 10% formalin solution and subjected for IHC study. The tissue dehydration during the IHC sample preparation leads to the shrinkage of the brain samples, which made pixel-to-pixel alignment of the images in both modalities challenging, but the presence of the suture allowed coarse alignment and assure that both IHC and OCT images were taken from approximately the same location (see Fig. 2).
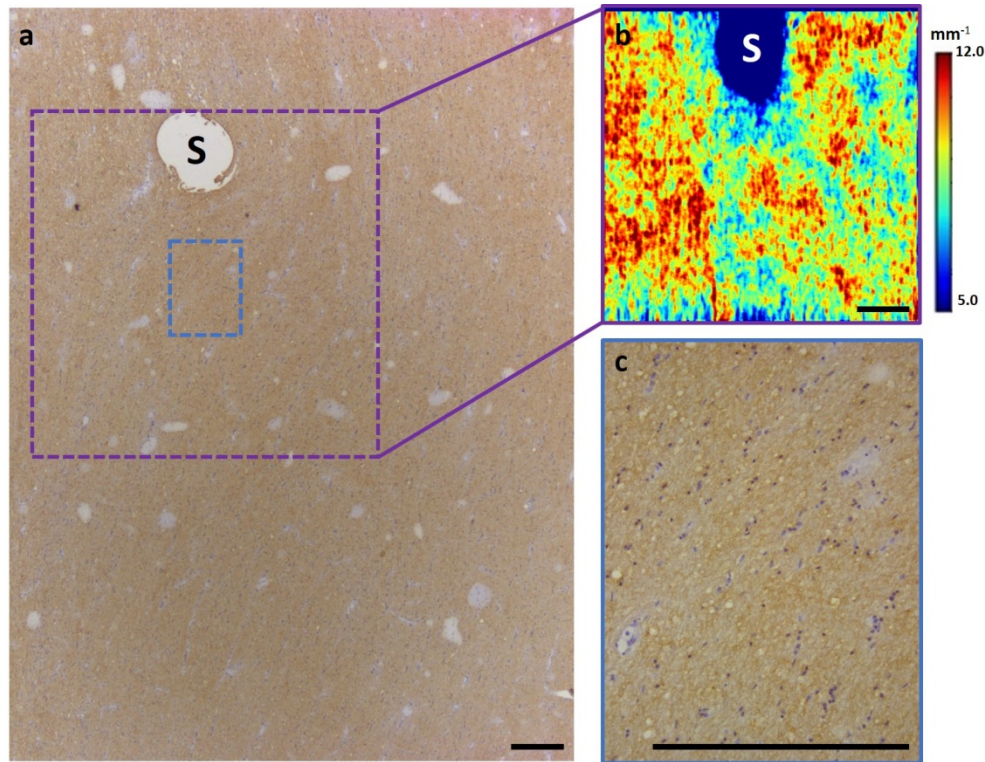
Fig. 2. Colocalization of the sites of OCT and IHC imaging. **a** – IHC image on x2.5 resolution; **b** – OCT image. The approximate site of the OCT image in the low resolution IHC image is delineated with purple rectangle. **c** - IHC image on x20 resolution. The site of the high resolution IHC image in the low resolution IHC image is delineated with blue rectangle. All scalebars are 400 μm.

The regions of interest were chosen in connection with their frequent involvement in tumor invasion process as well as under assumption of their morphological heterogeneity.

All samples were scanned by CP OCT device within 4-6 hours after the patients' deaths due to the protocol for establishing the onset of biological death and the procedure for conducting an autopsy and then subjected to histological examination using IHC staining (Fig. 3).

Both types of images – OCT (n = 64) and IHC (n = 68) – were quantitatively analyzed. Finally, the relationship between optical properties and morphological characteristics were established.

The study was approved by the Ethical Committee of the Privolzhsky Research Medical University (protocol No 6 dated 17.04.2019), and informed consent was obtained from each subject`s legal guardian. All methods were performed in accordance with the relevant guidelines and regulations.
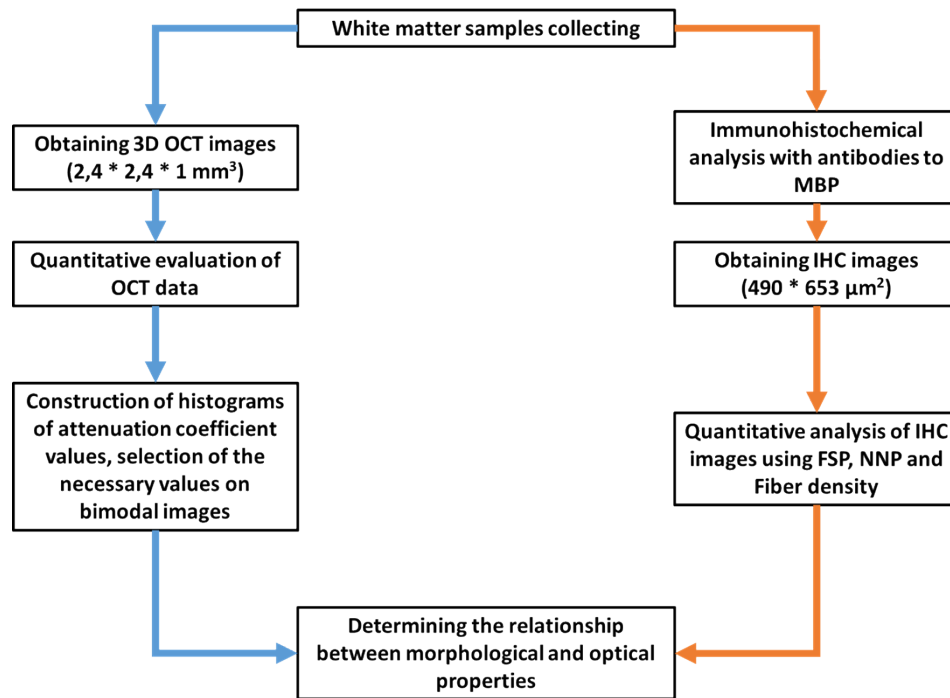
Fig. 3. Study design.

2.2. CP OCT device

The study was performed with a spectral-domain CP OCT device developed in the Institute of Applied Physics of the Russian Academy of Sciences (Nizhny Novgorod, Russia). CP OCT is a modification of polarization-sensitive OCT that allows recording changes in the state of polarization both due to birefringence and due to cross-scattering. As a result, two images are recorded simultaneously: an image in co-polarization (reflection of light with a polarization state parallel to the probe is detected) and an image in cross-polarization (only reflection of light with orthogonal polarization is detected). The sum of OCT signal intensities in both polarizations constitutes for full signal reflected from the sample and is not affected by the polarization effects. The CP OCT device has a common-path interferometric layout that operates at a 1.3 µm central wavelength with axial and lateral resolutions of 10 µm and 15 µm in air, respectively. It has a 20,000 A-scan/s scanning rate and performs 2D lateral scanning with a range of 2.4×2.4 mm^2 (256×256 A-scans) to obtain a 3D distribution of backscattered light in the polarization parallel and orthogonal to the polarization of the probing beam. Acquisition of each 3D OCT volume takes 26 seconds, while two-dimensional and en-face images in co- and cross-polarizations are separately visualized on a personal computer screen, as well as a three-dimensional image in the co- polarization. All images were collected using contactless scanning method. In total, the 64 3D CP OCT images were obtained and quantified (Fig. 3).

2.3. CP OCT data processing

Quantitative assessment of the OCT data was accomplished with the depth resolved approach that is derived from the assumption that the backscattering coefficient is proportional to the

attenuation coefficient with the constant ratio between the two in the OCT depth range [27]:

$$I_i \sim \alpha \cdot \mu_{att}(z_i) \cdot \exp\left[-2 \cdot \sum_{j=0}^{i} \mu_{att}(z_i) \cdot \Delta\right] \tag{1}$$

where I_i is the sum of OCT signal intensities in both polarization channels, μ_{att} is the specimen attenuation coefficient, z_i is the depth coordinate, Δ is the pixel size along the axial dimension.

In the present study, the method proposed in [28] was adopted. In comparison with the original work [27] the updated calculation approach rigorously accounts to the additive noise, which mitigates systemic attenuation coefficient underestimation in the high Signal-to-Noise Ratio (SNR) area and increase of the estimated attenuation coefficient value near the bottom of the image [21]. In this case, the depth-resolved attenuation coefficient can be written as:

$$
\begin{aligned}
\mu_i &= \frac{H_i \cdot SNR_i^{\mu}}{|H_i|^2 \cdot SNR_i^{\mu} + 1} \cdot \mu_i^{est} \\
H_i &= 1 - \frac{\sum\limits_{i+1}^{\infty} N_j}{\sum\limits_{i+1}^{\infty} I_j + \sum\limits_{i+1}^{i_{max}} N_j} = 1 - \frac{\langle N\rangle \cdot (i_{max} - i)}{\sum\limits_{i+1}^{\infty} I_j + \sum\limits_{i+1}^{i_{max}} N_j} \\
SNR_i^{\mu} &= \sum_{x_i, z_i \in W} \frac{\left|\mu_i^{est}\right|^2 - |N_i^{\mu}|^2}{|N_i^{\mu}|^2} \\
N_i^{\mu} &= \frac{N_i}{2\Delta \sum\limits_{i+1}^{i_{max}} (I_j + N_j)} = \frac{\langle N\rangle}{2\Delta \sum\limits_{i+1}^{i_{max}} (I_j + N_j)}
\end{aligned}
\tag{2}
$$

where $<N>$ is the amplitude of the noise floor, which can be estimated before the measurements, SNRiµ is the local signal-to-noise ratio (SNR) for the attenuation coefficient distribution, which is estimated by the averaging in the rectangular window with the side of W pixels. The W value should be sufficiently large (≥ 32 pixels) to provide sufficient statistics inside each window. The value $(I_j + N_j)$ is simply the measured signal at the depth j. Thus, all the values from Eq. (2) can be measured from the cross-sectional OCT intensity distributions. The attenuation coefficient was estimated in the 120-300 µm depth range. The en-face color-coded maps were built based on its values distribution for every OCT image.

One can note, that in the study the confocality of the OCT system and the spectral OCT roll-off were not taken into account. As been shown in [28], with the characteristics of the utilized OCT setup, the error for the attenuation coefficient estimation would not exceed 10%.

2.4. Immunohistochemical study

Brain samples were fixed in 10% formalin for 48 hours and a series of histological sections was made. Then IHC analysis was performed using antibodies to MBP (Abcam, USA). The staining technique is based on using the antibodies that are labeled with chromogen diaminobenzidine (DAB). As soon as antibodies bind with MBP, DAB polymerizes to form a light brown product, which allows the identification of myelinated fibers. Additionally, to reveal the cells nuclei the staining with hematoxylin was carried out. As a result of IHC staining it is possible to identify both myelinated fibers based on the DAB and cells nuclei based on hematoxylin.

Due to the use of a manual technique for conducting IHC studies, the intensity of staining was heterogeneous in different samples, which led to a necessity to perform visual assessment of the quality of staining of the sections. Samples with insufficient contrast of the myelinated fibers were screened out by an expert. (see Fig. 4 for an example of a sample with insufficient fibers contrast).

From each selected histological section, 3-4 images with a size of 490 * 653 µm were obtained. The region of interest in the sample was marked by stitching the brain tissue with a surgical
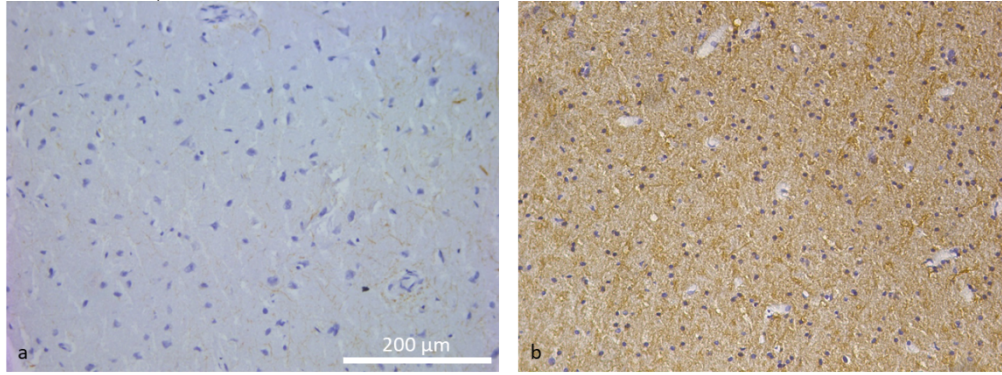
Fig. 4. a – an example of the IHC image screened out by an expert due to the low contrast of the fibers; b – an example of the IHC image included in the study.

suture (see Fig. 2). Although such approach does not allow exact match of the OCT and IHC images, it can guarantee that both were taken from the same area of approx. 5×5 mm. Note also that due to screening out of the low-quality IHC images, some OCT images do not have the IHC counterpart, but all IHC images do have a corresponding IHC image.

2.5. Quantitative evaluation of immunohistochemical images

To quantitatively access the morphological differences between white matter from different brain images, the IHC images were numerically evaluated. First, the images were transformed from RGB to optical density as follows [29]:

$$OD = -\log_{10}(RGB), \qquad (3)$$

where RGB is an RGB color vector with each component normalized to [0,1]. This transformation provides a space where a linear combination of stains will result in a linear combination of OD values [29]. This allows decomposition of the OD distribution into two stains, used for the IHC imaging as follows:

$$M_{sat} = Stain^{-1} \times OD, \qquad (4)$$

where M_{sat} is the matrix of stain saturations and Stain is the matrix of stain vectors. Such decomposition allows separation of fibers and nuclei images in the IHC image, as can be seen from the Fig. 5(a),(c),d.

The matrix of stain vectors was estimated for each IHC image separately. For this purpose, the OD distribution was transformed into spherical coordinates and scatterplot of the polar (θ) and azimuthal (φ) angles was analyzed (see Fig. 5(b)). Such a transformation allows simple heuristics to define the values corresponding to the two stains as follows:

$$\begin{aligned} DAB &= \varphi > percentile(\varphi, 99) \\ Hem &= \varphi < percentile(\varphi, 1) \end{aligned}, \qquad (5)$$

where DAB and Hem are points in the IHC image that were treated as points stained in the single dye (DAB and hematoxylin respectively). The stain vectors estimation was done with the averaging of the optical density of corresponding points. Note that the ultimate goal of the decomposition was separation of the fibers and nuclei in the IHC images, not the precise estimation of the stains. The concentration of the DAB dye was treated as the fibers image and concentration of the hematoxylin was treated as the nuclei image.
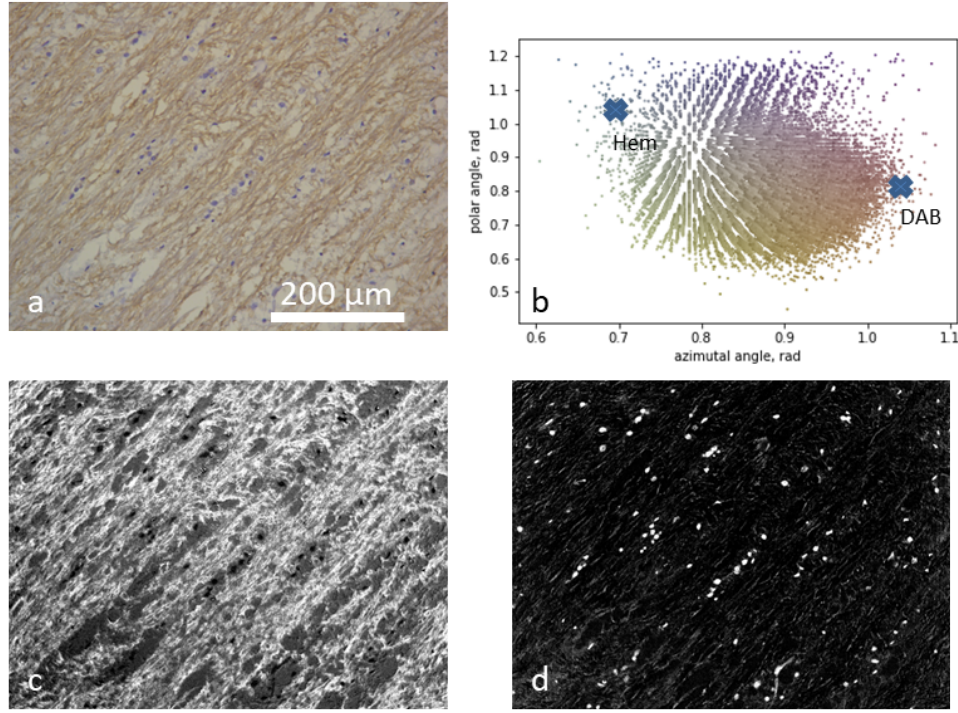
Fig. 5. IHC image decomposition into fibers and nuclei images. a – IHC image; b – IHC image pixel distribution in azimuthal angle - polar angle space with stains estimated according to Eq. (5) marked as crosses; c – image of the fibers; d – image of the nuclei.

The obtained fiber and nuclei images, (distributions of the corresponding stains concentrations) were binarized and analyzed. For nuclei analysis the total number of nuclei in the field of view was estimated. To numerically reveal the relevant difference in the fibers distribution, two parameters were utilized. Firstly, the fibers density, defined as the number of binarized fibers divided by the total area of the IHC image in pixels:

$$Dens = \frac{\sum_{i,j} B_{i,j}}{N_{image}}, \tag{6}$$

Where $B_{i,j}$ is the value of the pixel of the binarized fibers image, N_{image} is the total number of pixels in the IHC image. The second parameter was proposed to reflect the difference in the fibers distributions (see Fig. 6) from the thick bundles separated by relatively big gaps to the uniform mesh of thin fibers filling the whole field of view:

$$FSP = 0.5 \cdot \left(\sqrt{E[S_{row}^2] - (E[S_{row}])^2} + \sqrt{E[S_{column}^2] - (E[S_{column}])^2} \right)$$

$$S_{row} = \sum_{j=1...N_{column}} B_{i,j} \tag{7}$$

$$S_{column} = \sum_{i=1...N_{row}} B_{i,j}$$

where FSP is the proposed fiber structural parameter, E is the expected value function, $B_{i,j}$ is the value of the pixel of the binarized fibers image, N_{row}, N_{column} are number of pixels in rows and

columns of the IHC image respectively. As can be seen from the Fig. 6(e), the gaps and bundles structure of the fibers leads to the higher standard deviation of the total number of binarized pixels in the rows and columns of the image, which is easily quantified by the proposed parameter FSP.
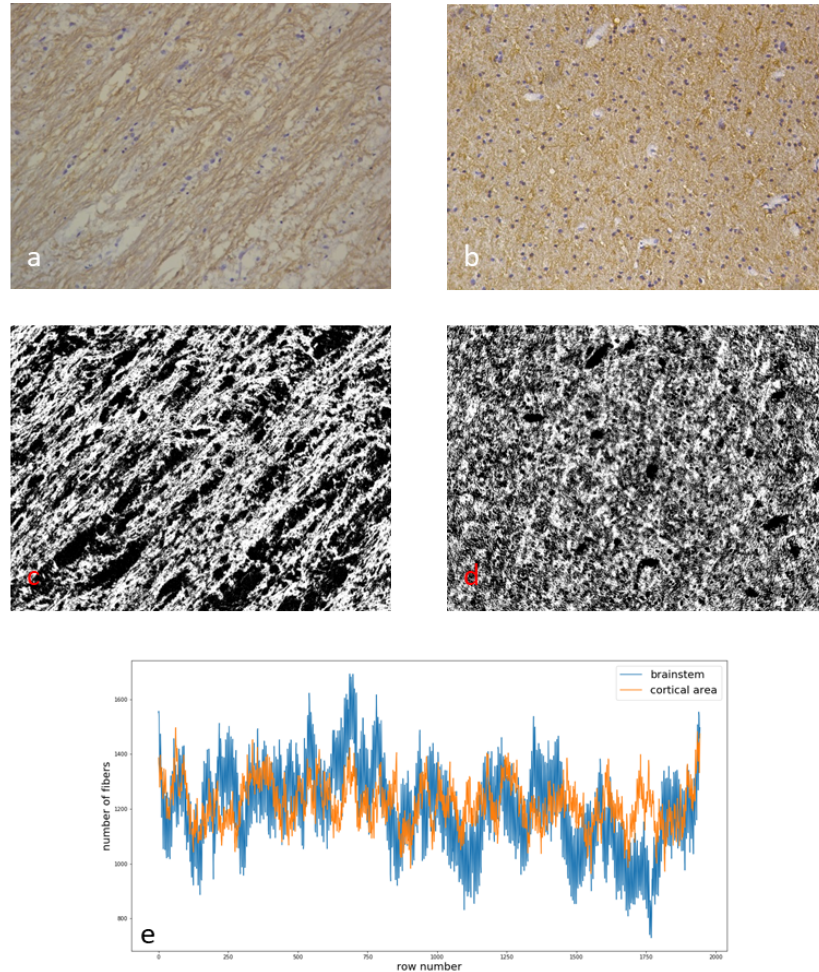

Fig. 6. FSP intuition. a,b – IHC images of the brain stem (a) and cortical area (b); c,d – binarized fibers in the panels a and b; e – total number of pixels equal to 1 in the rows as a function of the row number. The standard deviation of this value contributes to the proposed FSP according to eq (7).

2.6. Characteristic attenuation coefficient values in brain areas

To evaluate the characteristic attenuation coefficient value in each OCT image the 64-bin histogram of the value was constructed and the value of the rightmost maximum was taken as the characteristic attenuation coefficient value of the sample (Fig. 7(c), d). This approach was chosen to account for the bimodality of some of the images, which may arise from the presence of the stripes of gray matter in the tissue (2 samples) (example is presented on Fig. 7(a)), or the presence of the non-transparent object (surgical suture), inserted in the sample for the convenience of the navigation in the sample (17 samples) (example can be seen on Fig. 7(b)). The rest of the samples

showed single-mode behavior, and for these samples the selected approach for characteristic attenuation coefficient value evaluation gives close results with the mean and median attenuation coefficient values in the sample.
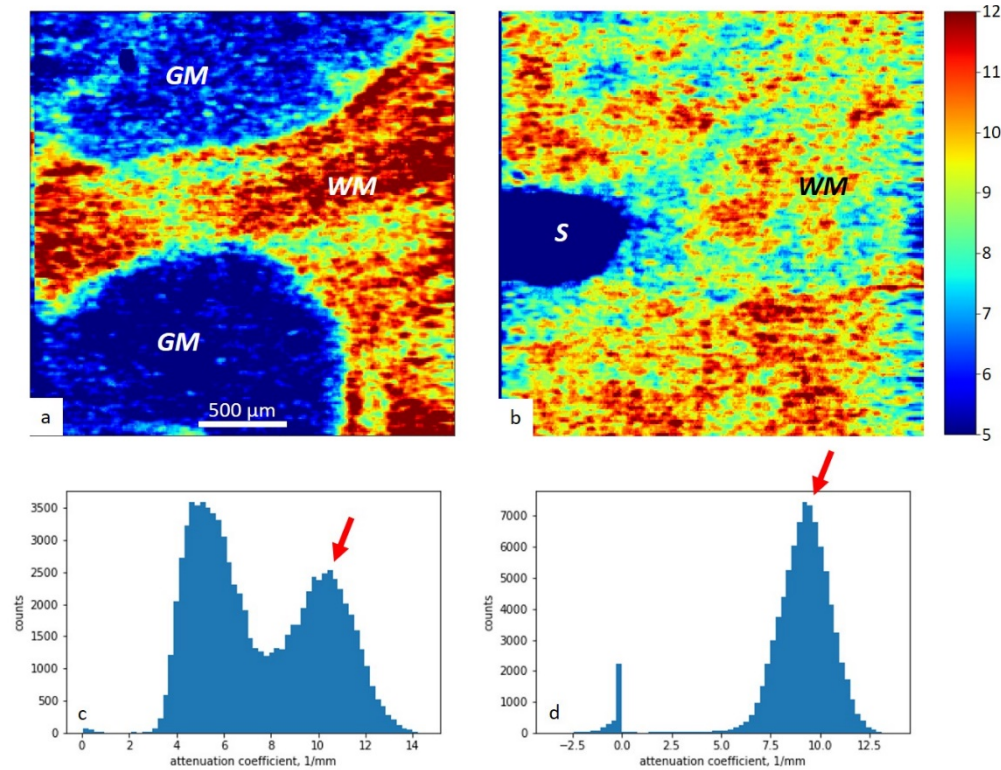
Fig. 7. Characteristic attenuation coefficient value estimation in case of the bimodal distribution. a – images of the white matter (WM) entangled with the gray matter (GM); b – image of the white matter with the non-transparent object (surgical suture) inserted in the field-of-view (S); c,d – correspondent histograms with the red arrows indicating the obtained characteristic attenuation coefficient values.

2.7. Relation of the attenuation coefficient and IHC numerical features

To derive the relationship between the attenuation coefficient calculated from the OCT data and the IHC quantitative parameters, only OCT images with the corresponding IHC images were selected. Note that because some of the IHC images turned out to be with insufficient contrast and were screened out by an expert, some of the OCT images did not have the corresponding IHC image and some OCT images have several corresponding IHC images. In total 24 samples were selected for this part of the study with corresponding 68 IHC images. All possible sets of the attenuation coefficient and IHC characteristics values were formed for each set of images taken from the same sample near the same marker (surgical suture). In total, 154 values sets were formed this way.

2.8. Statistical analysis

The statistical analysis pursued several goals. Firstly, the difference of the measured attenuation coefficient and IHC quantitative characteristics between investigated brain areas was evaluated the Mann-Whitney U test. The null hypothesis that for the randomly selected samples from two brain

areas the probability of the sample from the brain area one been greater than the sample from the brain area two is equal to the probability of the sample from the brain area two been greater than the sample from the brain area one was tested. As an alternative hypothesis the statement that for randomly selected samples from two brain areas the probability of the sample from the brain area one been greater than the sample from the brain area two is greater than the probability of the sample from brain area two been greater than the sample from brain area one was tested. Note that such one-sided test aims not only to establish statistically significant difference between two brain areas, but also to establish which brain area has measured values been stochastically greater than values in the other brain area. Thus, such a test produces asymmetric results for any pair of brain areas: if the values in brain area one are bigger than the values in the brain area two with statistical significance, the opposite statement (values in brain area two are greater than values in brain area one) is false and should be rejected with high probability.

The next goal of the statistical analysis was to establish correlations between all the measured values, both OCT-based and IHC-based. The correlations between the estimated attenuation coefficient and quantitative IHC characteristics were established with partial correlations, which allows one to estimate the correlation between two variables while controlling for the other variables. The set of three IHC quantitative characteristics was evaluated with variance inflation factor (VIF) [30]. The VIF value establishes how well one variable from the set can be represented as a linear combination of the other variables. If VIF value is high (the cut-off of 5 is commonly used), one can conclude that the multicollinearity in the dataset is high, i.e. some of the values in the dataset are mere linear combination of the other variables.

Lastly, the dependence of the attenuation coefficient on the IHC quantitative characteristics was established and the importance of each of IHC characteristics on the prediction of the attenuation coefficient was analyzed. The attenuation coefficient was represented as a linear combination of the standardized quantitative IHC characteristics using ordinary least squares regression. In case of the variables standardization before the regression (i.e. subtraction of the mean a scaling to the unit variance) the obtained regression coefficient can be treated as an importance of the correspondent variable to the prediction of the dependent variable. Note that this statement is true only if the multicollinearity among the independent variables is low. The quality of the linear regression was accessed with the coefficient of determination (R^2) [30] which shows how much of the variance of the independent variable is accounted with the predictions of the model. For linear least squares multiple regression with an estimated intercept term, R^2 equals the square of the Pearson correlation coefficient between the observed and predicted data points. The impact of each of three IHC quantitative characteristics was also evaluated with the permutation importance method [31]. The feature importance is defined as the drop in the metric of the predictor performance (e.g. R^2) when the values of the feature are randomly permutated. The bigger the drop, the more important the variable for the predictor performance. Note, that this approach also gives relevant results only in case of low multicollinearity among the independent variables.

3. Results

3.1. Comparison of depth-resolved and log-and-linear-fit methods for attenuation coefficient estimations

To compare conventional approach of attenuation coefficient estimation from OCT data the data from a uniform scattering plastic sample was collected and attenuation coefficient was estimated with both log-and-linear-fit method and the depth-resolved method, calculated according to the Eq. (2). As one can see from Fig. 8, both methods leads to the same value of the attenuation coefficient.

In Fig. 9 one color-coded maps of the attenuation coefficient distribution in the brain sample obtained with two methods in the same depth ranges are shown. One can see better contrast and
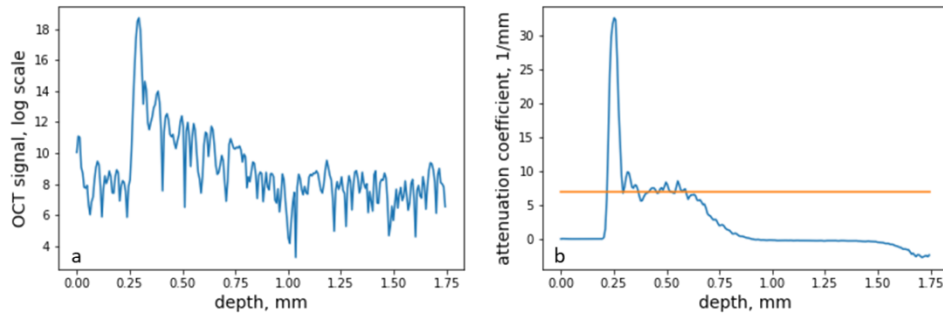
Fig. 8. a – OCT A-scan of the sample with uniform scattering coefficient; **b** – attenuation coefficient of the sample estimated with the depth-resolved method (blue line) and log-and-linear-fit approach (yellow line).

signal-to-noise for the maps obtained with the depth-resolved method for all depth ranges. The improved quality of the color-coded maps allows bigger number of fine details of the object to be clearly visualized.
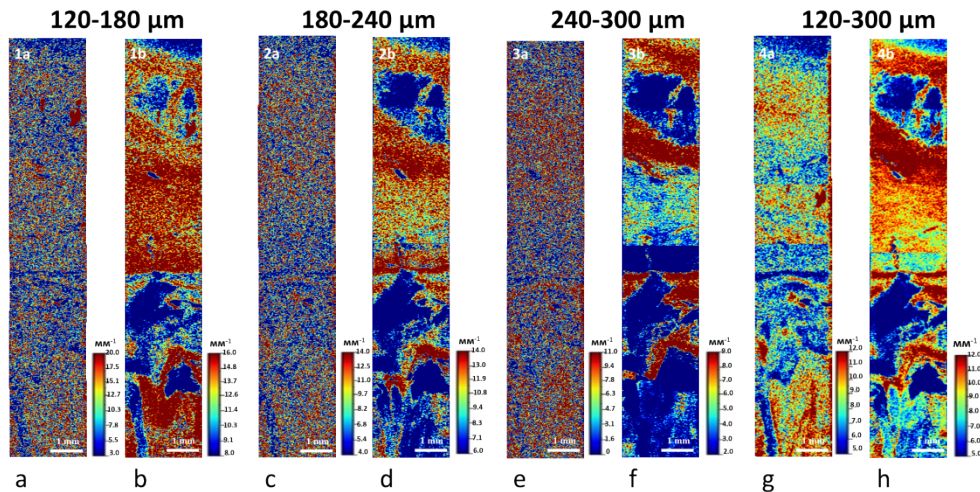

Fig. 9. Color-coded maps of the brain sample, obtained with log-and-linear-fit approach (panels a,c,e,g) and the depth-resolved approach (panels b,d,f,h) in the same depth range.

3.2. Morphological differences of white matter from different brain regions

The morphological differences between white matter samples from different brain regions can be accessed both qualitatively (see Fig. 6) and quantitatively (Table 1–3; note that the Tables show the results of on-sided test, i.e. not only shows that the values are different for the brain areas in the row and in the column, but that the values for the areas in the row are greater than the values for the area in the column). Visual analysis allows differentiating regions with large parallel fibers, separated by interspaces (Fig. 10(a)), regions with densely packed thin fibers, forming a network structure (Fig. 10(d), (e)) as well as areas, characterized by both parallel and chaotically arranged fibers (Fig. 10(b), (c)). The use of FSP makes it possible to differentiate almost all the studied areas among themselves, with the exception of the pairs of cortical area-subcortical area,

brainstem-corpus callosum and capsula interna-corpus callosum (Table 1). The areas that cannot be delineated using FSP can be distinguished by using NNP (Table 2), which emphasizes the importance of using these parameters in conjunction. The presence of the region-specific set of FSP and NNP values is more evident from the Fig. 10(f), where all the selected brain areas form separable clusters in the space of the proposed IHC quantitative parameters. As can be seen from the Tables 1, 2 and Fig. 10(f), all the samples pairs can be separated from each other with high accuracy.
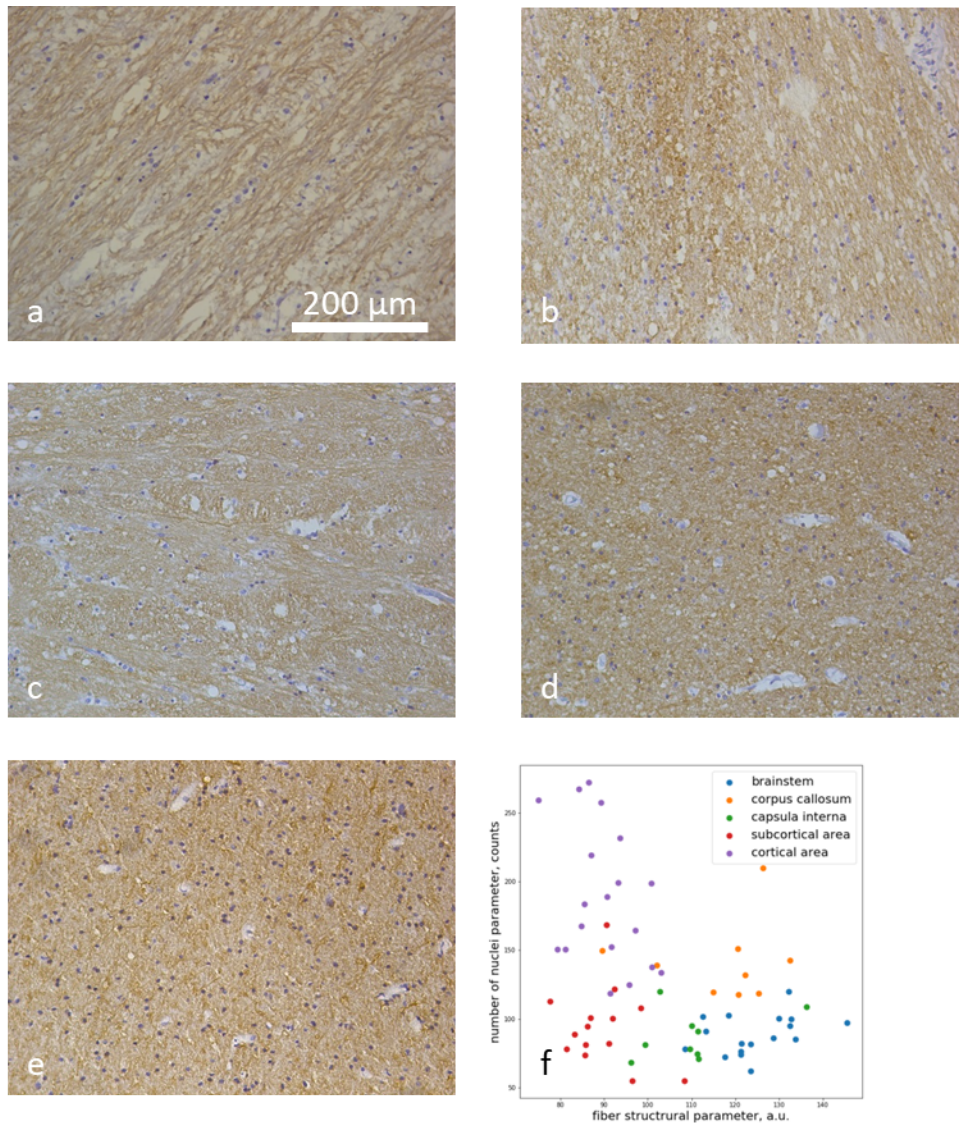
Fig. 10. Characteristic examples of the IHC images of the studied brain areas. a – brainstem; b – corpus callosum; c – capsula interna; d – subcortical area; e – cortical area. f – distributions of the calculated IHC numerical characteristics for the studied brain areas.

From Table 3 one can see that only brainstem has statistically lower fiber density in comparison with other brain areas, while the values for the fiber density in all investigated brain areas lie in

Table 1. Comparison of FSP of different white matter regions[a]

	Cortical area (n = 19) 90.8 [85.2; 94.7][a]	Subcortical area (n = 14) 88.7 [85.7; 92.3]	Capsula Interna (n = 9) 110.0 [102.8;111.5][a]	Corpus Callosum (n = 9) 120.7 [115.0;125.3][a]	Brainstem (n = 17) 123.5 [118.4; 132.1][a]
Cortical area (n = 19)	-	0.39	0.99	0.99	0.99
Subcortical area (n = 14)	0.62	-	0.99	0.99	0.99
Capsula Interna (n = 9)	**$7*10^{-5}$**	**$1*10^{-4}$**	-	0.94	0.99
Corpus Callosum (n = 9)	**$1*10^{-4}$**	**$3*10^{-4}$**	0.07	-	0.88
Brainstem (n = 17)	**$2*10^{-7}$**	**$1*10^{-6}$**	**$2*10^{-3}$**	0.13	-

[a]P-values for the alternative hypothesis of the Mann-Whitney U test that the FSP values for the brain areas in the tables' raw been stochastically greater than the values for the brain areas in the tables' column are presented with p < 0.05 been highlighted and underlined; [a]Me [Q1; Q3]: Me – median; [Q1;Q3] – 25th and 75th percentiles values respectively.

Table 2. Comparison of NNP values of different white matter regions[a]

	Cortical area (n = 19) 183 [150; 225][a]	Subcortical area (n = 14) 91 [79; 106]	Capsula Interna (n = 9) 81 [74; 95][a]	Corpus Callosum (n = 9) 139 [119; 149][a]	Brainstem (n = 17) 86 [78; 100][a]
Cortical area (n = 19)	-	**$4*10^{-6}$**	**$1.8*10^{-5}$**	**0.007**	**$2*10^{-7}$**
Subcortical area (n = 14)	0.99	-	0.27	0.99	0.32
Capsula Interna (n = 9)	0.99	0.75	-	0.99	0.70
Corpus Callosum (n = 9)	0.99	**$6*10^{-4}$**	**$5*10^{-4}$**	-	**$4*10^{-5}$**
Brainstem (n = 17)	0.99	0.69	0.31	0.99	-

[a]P-values for the alternative hypothesis of the Mann-Whitney U test that the NNP values for the brain areas in the tables' raw been stochastically greater than the values for the brain areas in the tables' column are presented with p < 0.05 been highlighted and underlined; [a]Me [Q1; Q3]: Me – median; [Q1;Q3] – 25th and 75th percentiles values respectively.

Table 3. Comparison of fiber density values of different white matter regions[a]

	Cortical area (n = 19) 0.47 [0.46; 0.48][a]	Subcortical area (n = 14) 0.48 [0.47; 0.5]	Capsula Interna (n = 9) 0.48 [0.47;0.49][a]	Corpus Callosum (n = 9) 0.47 [0.46;0.48][a]	Brainstem (n = 17) 0.46 [0.45; 0.464]
Cortical area (n = 19)	-	0.99	0.95	0.54	**$6*10^{-4}$**
Subcortical area (n = 14)	**$5*10^{-3}$**	-	0.51	0.25	**$4*10^{-2}$**
Capsula Interna (n = 9)	0.055	0.77	-	0.14	**$4*10^{-5}$**
Corpus Callosum (n = 9)	0.48	0.96	0.87	-	**$2*10^{-3}$**
Brainstem (n = 17)	0.99	0.99	0.99	0.98	-

[a]P-values for the alternative hypothesis of the Mann-Whitney U test that the fiber density values for the brain areas in the tables' raw been stochastically greater than the values for the brain areas in the tables' column are presented with $p < 0.05$ been highlighted and underlined; [a]Me [Q1; Q3]: Me – median; [Q1;Q3] – 25th and 75th percentiles values respectively.

the relatively narrow range of values (0.45-0.5 for the smallest value of the Q1 and the biggest value of the Q3 respectively).

3.3. Optical properties of white matter from different brain regions

For each 3D OCT image attenuation coefficient values were calculated. Median values of the studied white matter groups are presented in the Table 4. It can be seen that maximum values of the attenuation coefficient were obtained for the cortical area (10.6 [9.9; 11.9] mm^{-1}), and this region is significantly different from other brain areas: subcortical area (9.5 [8.8; 10.4] mm^{-1}, p = 0.009), capsula interna (8.9 [7.5; 9.4] mm^{-1}, p = 0.0005), corpus callosum (9.1 [8.3; 9.2] mm^{-1}, p = 0.005) and brainstem (8.7 [8.5; 9.2] mm^{-1}, p = 0.001).

Table 4. Comparison of Attenuation coefficient values of different white matter regions calculated by depth-resolved method[a]

	Cortical area (n = 14) 10.6 [9.9; 11.9] mm^{-1} [a]	Subcortical area (n = 22) 9.5 [8.8; 10.4] mm^{-1}	Capsula Interna (n = 10) 8.9 [7.5; 9.4] mm^{-1} [a]	Corpus Callosum (n = 8) 9.1 [8.3; 9.2] mm^{-1} [a]	Brainstem (n = 10) 8.7 [8.5; 9.2] mm^{-1} [a]
Cortical area (n = 14)	-	**0.009**	**0.0005**	**0.005**	**0.001**
Subcortical area (n = 22)	0.99	-	**0.029**	0.1	**0.035**
Capsula Interna (n = 10)	0.99	0.97	-	0.77	0.66
Corpus Callosum (n = 8)	0.99	0.91	0.25	-	0.44
Brainstem (n = 10)	0.99	0.97	0.37	0.59	-

[a]P-values for the alternative hypothesis of the Mann-Whitney U test that the attenuation coefficient values for the brain areas in the tables' raw been stochastically greater than the values for the brain areas in the tables' column are presented with $p < 0.05$ been highlighted and underlined;[a]Me [Q1; Q3]: Me – median; [Q1;Q3] – 25th and 75th percentiles values respectively.

The result of pairwise comparison of selected white matter areas based on their attenuation coefficient values is presented in Table 3.

3.4. *Partial correlations between attenuation coefficient and quantitative IHC characteristics*

On the dataset of 154 synthetic datapoints, created according to subsection 2.5, partial correlations were calculated for the attenuation coefficient and each of the three quantitative IHC characteristics and are presented in Table 5.

Table 5. Partial correlation of the attenuation coefficient [a]

	FSP	Number of nuclei	Fiber density
Attenuation coefficient	-0.49; [-0.61, -0.37]; $7*10^{-11}$	0.29; [0.14, 0.43]; $3*10^{-4}$	-0.09; [-0.25, 0.07]; 0.25

[a]Partial correlations for the attenuation coefficient with the IHC quantitative parameters controlling for the other two parameters. 95% confidence interval and p-value for the partial correlations are also presented as **p_corr; [ci_low, ci_high]; p-value**.

To ensure low multicollinearity among IHC quantitative parameters, variation inflation factor was calculated for the set of three IHC parameters and presented in Table 6:

Table 6. Variation inflation factor[a]

	FSP	Number of nuclei	Fiber density
VIF	1.44	1.22	1.21

[a]Variation inflation factor for the IHC quantitative parameters.

The VIF value has the range from 1 to infinity, where 1 means no multicollinearity in the data and the threshold value of 5 is conventionally used as an indicator for high multicollinearity. As one can see from the Table 6, the multicollinearity among the quantitative IHC characteristics is low and can be neglected in further analysis.

3.5. *Attenuation coefficient linear regression on IHC quantitative characteristics*

Attenuation coefficient value can be represented as a linear combination of quantitative IHC parameters with linear regression. To be able to treat the linear regression coefficients as the weights of the corresponding variables in the linear prediction model, all variables were standardized before fitting the model. The predicted values of the attenuation coefficient based on the IHC quantitative characteristics can be written as:

$$\text{Att}_{pred} = C_{fsp} \times FSP' + C_{nucl} \times NNP' + C_{dens} \times Dens' + C_0$$
$$FSP' = \frac{FSP - mean_{FSP}}{std_{FSP}}$$
$$NNP' = \frac{NNP - mean_{NNP}}{std_{NNP}} \qquad , \qquad (8)$$
$$Dens' = \frac{Dens - mean_{Dens}}{std_{Dens}}$$

where Att_{pred} is the predicted value of the attenuation coefficient, FSP – fiber structural parameter, $mean_{FSP}$ – mean value of the FSP, std_{FSP} – is the standard deviation of the FSP; NNP – number of nuclei parameter, $mean_{NNP}$ – mean value of the NNP, std_{NNP} – is the standard deviation of the NNP; Dens – fiber density parameter, $mean_{Dens}$ – mean value of the fiber density, std_{Dens} – is the standard deviation of the fiber density; C_0 is the constant intercept term. The coefficients were found to minimize of the mean squared between measured and predicted attenuation coefficients. The coefficients values are presented in Table 7:

Since the multicollinearity among the IHC quantitative characteristics was low, the absolute values of these coefficients can be treated as weights of the correspondent variable in the resulting prediction of the attenuation coefficient.

Table 7. Linear regression coefficients for the three variables linear model

	FSP	Number of nuclei	Fiber density	Intercept
Coefficient value	-0.62	0.30	-0.09	9.85

The quality of the prediction model was accessed with the coefficient of determination (R^2) which for the three parameter linear model was equal to 0.415, which can be understood as 40% of the attenuation coefficient variance was predicted based on linear combination of IHC quantitative characteristics.

The importance of the variables on the prediction was also analyzed with permutation importance method [31]. For this metrics the target independent variable was randomly permuted and with the other two intact variables plugged into the linear regression model. The more the R^2 value of the predictions based on the permuted variable drops in comparison with the R^2 of the prediction based on all three intact variables, the more important this variable for the model performance. In Table 8 one can see the permutation importance of all three IHC quantitative characteristics for the prediction of the attenuation coefficient as a relation of the differences in R^2 before and after the permutation divided by the R^2 before the permutation.

Table 8. Variables permutation importance for the three variables linear model

	FSP	Number of nuclei	Fiber density
Permutation importance	1.4	0.35	0.02

Permutation importance of IHC quantitative characteristics represented as a relation of the differences in R2 before and after the permutation divided by the R2 before the permutation.

The permutation importance greater than 1 means that some of the permutation leads to the predictions to have negative correlation with the estimated attenuation coefficients values.

The scatterplots for all the IHC parameters vs the attenuation coefficient estimated from the OCT data as well as the attenuation coefficient estimated from the IHC parameters with the linear model vs the attenuation coefficient estimated from the OCT data are presented in Fig. 11.

The linear model based only on FSP and number of nuclei parameters was also built using mean squared error minimization and the same analysis of feature importance was performed. The R^2 value for the two parameter linear model was 0.41. The coefficients values and the permutation importance are presented in Tables 9 and 10 respectively.

Table 9. Linear regression coefficients for the two variables linear model

	FSP	Number of nuclei	Intercept
Coefficient value	-0.58	0.30	9.85

Table 10. Variables permutation importance for the two variables linear model[a]

	FSP	Number of nuclei
Permutation importance	1.20	0.36

[a]Permutation importance of IHC quantitative characteristics represented as a relation of the differences in R2 before and after the permutation divided by the R2 before the permutation.
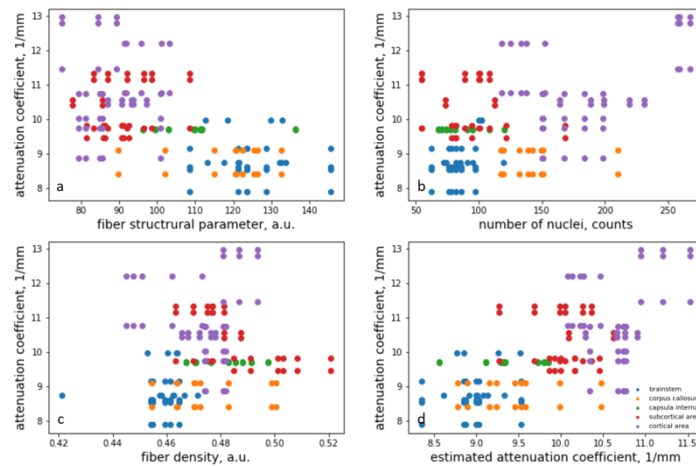
Fig. 11. The dependence of the attenuation coefficient on the IHC quantitative parameters (a-c) and the attenuation coefficient estimated from the IHC parameters with the linear model vs the attenuation coefficient estimated from the OCT data (d).

4.　Discussion

The development of methods for *in vivo* visualization of white matter and obtaining information about its morphological features in real time is an important task, which solution will improve the neurosurgical care to patients, as well as give impetus to experimental research aimed at studying diseases associated with damage to myelinated fibers. In this study, for the first time we have discovered the relationship between optical properties of the white matter of the brain and its morphological features.

　All the characteristics, calculated in the present study suggest the same conclusion: mean number of fibers in the IHC images, calculated as a relation of the area occupied by the fibers to the total area of an IHC image is a far less important parameter for predicting the attenuation coefficient than the proposed fiber structural parameter and the number of nuclei. Fiber density has approximately 5 times smaller partial correlation with the estimated attenuation coefficient than the other two parameters, has approximately 5 times smaller weight in the linear regression model and random permutation of the fiber density leads to only 2.1% drop in the coefficient of determination of the model. The other two parameters show comparable importance to the attenuation coefficient distribution according to all of the used metrics. Complete exclusion of the fiber density parameter from the linear model leads only to slight drop in performance from coefficient of determination of 0.415 to 0.410 (one should recall, that in case of mean squared error minimization coefficient of determination is the Pearson correlation between the predicted value and the prediction). Note that it was impossible to plot the predictions from the 3 parameters model and the two parameters model in a way that they will become distinguishable in the figure. Such an apparent absence of the attenuation coefficient dependence from the fiber density can be explained by the fact that the range of the fiber density values in the collected dataset was small as can be seen from the Table 3. Thus, the dependence on the fiber density could not be established from the dataset used in the study and more brain samples with wider range of fiber density values should be used. However, the study suggests that the proposed Fiber Structural Parameter together with the number of nuclei could be used as a predictor for the sample attenuation coefficient.

　The obtained dependences between the IHC quantitative parameters and attenuation coefficient, estimated from the OCT data have a straightforward interpretation: the more scatterers a brain area

has, the stronger the scattering from this brain area is. While the NNP has a clear interpretation as a number of scatterers, the connection between the FSP and the number of scatterers in the volume is less intuitive. The FSP grows with the number and size of empty spaces between the fibers bundles, while the lower value indicated more uniform fill of the field-of-view with the fibers. Since the total number of fibers in the field-of-view was the same in all of the studied brain areas, the voids-and-bundles structure (as in the brainstem) leads to the areas of small number of refractive index changes both in the voids and in the bundles, while uniform fill of the field-of-view with fibers leads to its uniform fill with the refractive index changes. These changes act as scattering centers, thus the higher value of the FSP corresponds to the lower number of scatterers and visa-versa. These influence of the morphological structure to the value of the attenuation coefficient has good correspondence with the statistically significant differences in the attenuation coefficient values between the superficial white matter structures (cortical and subcortical areas) and deep white matter structures (brainstem, corpus callosum and capsula interna), as can be seen from the Tables 1–4. The difference in the function of these areas leads to the difference in their morphological structures, which, in turn, leads to the differences in their scattering properties and attenuation coefficient values.

The discovered dependencies between attenuation coefficients and IHC quantitative parameters allow conclusions about the morphological state of the investigated area of the white matter, both in terms of the number of nuclei and the structure of the myelinated fibers. This discovery opens the opportunity for the usage of the OCT as a neuronavigation tool.

One should also note, that the proposed process for the derivation of the relation between the IHC numerical characteristics and the attenuation coefficient, estimated from the OCT data, will give valid useful results only in the case that the correlation between the parameters in every group has the same sign (or equals to zero). If this hypothesis holds, the generated samples, with independent values in two modalities (IHC and OCT), represent the worst-case scenario in terms of the Pearson coefficient absolute value, i.e. any correlation within the groups of the same sign as a global trend correlation will lead to the increase of the Pearson coefficient absolute value. If the hypothesis does not hold, i.e. there are some groups with the correlation between the values measured in two modalities (IHC and OCT) of the opposite sign from the global trend correlation, one should admit that the so called Simpson's paradox [32] is taken place and the proposed analysis is inapplicable in this case. Additional experiments with the same samples visualized in both modalities are required to assert the presence of the global trend.

The limitations of our study are mainly related to three different problems. First, it should be emphasized that the study was carried out on post-mortem samples of the human brain, due to the impossibility of conducting intraoperative examination of a number of areas and the impossibility of taking samples of healthy brain tissue for histological examination. The amount of collected samples is limited due to ethical considerations. In this regard, the continuation of experiments with a larger amount of samples is required to confirm the obtained results. The second point that should be mentioned is the inability to accurately compare the IHC and OCT images. We tried to overcome this drawback by generating synthetic samples with both types of measurements, which is described in detail in section 2.5. Unfortunately, it is unlikely to overcome the significant difference in the size of images obtained by different methods. However, it is possible to adjust the study protocol in order to mark each area where OCT data were obtained for subsequent collecting of IHC images. The third limitation is associated with the process of preparation and staining of histological sections. On the one hand, a slight change in the morphological properties of tissue samples is possible during the preparation of histological sections, in particular, the occurrence of dehydration when the samples are fixed in a formalin solution [33], which may slightly distort the true morphological picture. On the other hand, as mentioned above, the use of a manual technique for staining sections causes uneven staining, leading to the need to sort the sections. Perhaps the use of a hardware technique will overcome this problem.

5. Conclusion

Statistically significant correlation between morphological features of white matter based on the quantitative evaluation of IHC images and its optical properties based on attenuation coefficient estimated from OCT data was found. It was shown that commonly underlooked factors such as number of nuclei and the arrangement of myelinated fibers strongly affect the attenuation coefficient of the brain sample. The linear combination of the proposed quantitative characteristics describing these morphological features accounts for 41% of the attenuation coefficient variance in the collected dataset. The discovered dependencies between attenuation coefficients and IHC quantitative parameters allow conclusions about the morphological state of the investigated area of the white matter. This discovery opens the opportunity for the usage of the OCT as a neuronavigation tool.

Disclosures. The authors declare no conflicts of interest.

Data Availability. Data underlying the results presented in this paper are not publicly available at this time but may be obtained from the authors upon reasonable request.

References

1. S. Wang, X. Chen, W. Wu, Z. Chen, H. Du, X. Wang, Y. Fu, L. Hu, and J. Chen, "Rapid, label-free identification of cerebellar structures using multiphoton microscopy," J. Biophotonics **10**(12), 1617–1626 (2017).
2. M. J. Farrar, F. W. Wise, J. R. Fetcho, and C. B. Schaffer, "In vivo imaging of myelin in the vertebrate central nervous system using third harmonic generation microscopy," Biophys. J. **100**(5), 1362–1371 (2011).
3. C. Kut, K. L. Chaichana, J. Xi, S. M. Raza, X. Ye, E. R. McVeigh, F. J. Rodriguez, A. Quinones-Hinojosa, and X. Li, "Detection of human brain cancer infiltration ex vivo and in vivo using quantitative optical coherence tomography," Sci. Transl. Med. **7**(292), 292ra100 (2015).
4. K. S. Yashin, E. B. Kiseleva, A. A. Moiseev, S. S. Kuznetsov, L. B. Timofeeva, N. P. Pavlova, G. V. Gelikonov, IA Medyanik, L. Y. Kravets, E. V. Zagaynova, and N. D. Gladkova, "Quantitative nontumorous and tumorous human brain tissue assessment using microstructural co- and cross-polarized optical coherence tomography," Sci. Rep. **9**(1), 2024 (2019).
5. P. Morell, *Myelin*, 1st ed. (Plenum Press, 1984).
6. J. M. Edgar and I.R. Griffiths, "White matter structure: a microscopist's view," in *Diffusion MRI*, 2nd ed. (Academic Press, 2009), pp. 74–103.
7. F. Aboitiz, A. B. Scheibel, R. S. Fisher, and E. Zaidel, "Fiber composition of the human corpus callosum," Brain Res. **598**(1-2), 143–153 (1992).
8. A. Wada, J. Goto, N. Goto, N. Kawamura, and K. Matsumoto, "Are there one million nerve fibres in the human medullary pyramid?" Okajimas Folia Anat. Jpn **77**(6), 221–224 (2001)..
9. A. Schüz and V. Braitenberg, "The human cortical white matter: quantitative aspects of cortico-cortical long-range connectivity," in *Cortical Areas: Unity and Diversity*, A. Schüz and R. Miller, eds. (Taylor & Francis, 2002), pp. 377–385.
10. M. Mancini, G. Giulietti, N. Dowell, B. Spanò, N. Harrison, M. Bozzali, and M. Cercignani, "Introducing axonal myelination in connectomics: A preliminary analysis of g-ratio distribution in healthy subjects," NeuroImage **182**, 351–359 (2018).
11. C. S. von Bartheld, J. Bahney, and S. Herculano-Houzel, "The search for true numbers of neurons and glial cells in the human brain: A review of 150 years of cell counting," J Comp Neurol **524**(18), 3865–3895 (2016).
12. Y. Fan, Y. Xia, X. Zhang, Y. Sun, J. Tang, L. Zhang, and H. Liao, "Optical coherence tomography for precision brain imaging, neurosurgical guidance and minimally invasive theranostics," Biosci. Trends **12**(1), 12–23 (2018).
13. J. Ben Arous, J. Binding, J. F. Leger, M. Casado, P. Topilko, S. Gigan, A. C. Boccara, and L. Bourdieu, "Single myelin fiber imaging in living rodents without labeling by deep optical coherence microscopy," J. Biomed. Opt. **16**(11), 116012 (2011).
14. H. Wang, T. Akkin, C. Magnain, R. Wang, J. Dubb, W. J. Kostis, M. A. Yaseen, A. Cramer, S. Sakadžić, and D. Boas, "Polarization sensitive optical coherence microscopy for brain imaging," Opt. Lett. **41**(10), 2213–2216 (2016).
15. H. Nakaji, N. Kouyama, Y. Muragaki, Y. Kawakami, and H. Iseki, "Localization of nerve fiber bundles by polarization-sensitive optical coherence tomography," J. Neurosci. Methods **174**(1), 82–90 (2008).
16. H. Wang, J. Zhu, M. Reuter, L. N. Vinke, A. Yendiki, D. A. Boas, B. Fischl, and T. Akkin, "Cross-validation of serial optical coherence scanning and diffusion tensor imaging: a study on neural fiber maps in human medulla oblongata," NeuroImage **100**, 395–404 (2014).
17. K. S. Yashin, E. B. Kiseleva, E. V. Gubarkova, A. A. Moiseev, S. S. Kuznetsov, P. A. Shilyagin, G. V. Gelikonov, I. A. Medyanik, L. Y. Kravets, A. A. Potapov, E. V. Zagaynova, and N. D. Gladkova, "Cross-polarization optical coherence tomography for brain tumor imaging," Front. Oncol **9**, 201 (2019).

18. S. A. Boppart, J. M. Herrmann, C. Pitris, B. E. Bouma, G. J. Tearney, M. E. Brezinski, and J. G. Fujimoto, "Interventional optical coherence tomography for surgical guidance," in *Proceedings of the Conference on Lasers and Electro-Optics Europe - Technical Digest* (1998), pp. 123–124.

19. H. J. Böhringer, E. Lankenau, F. Stellmacher, E. Reusche, G. Hüttmann, and A. Giese, "Imaging of human brain tumor tissue by near-infrared laser coherence tomography," Acta Neurochir **151**(5), 507–517 (2009).

20. A. Giese, H. J. Böhringer, J. Leppert, S. Kantelhardt, E. Lankenau, P. Koch, R. Birngruber, and G. Hüttmann, "Non-invasive intraoperative optical coherence tomography of the resection cavity during surgery of intrinsic brain tumors," Proc. SPIE **6078**, 60782Z (2006).

21. M. Almasian, L. S. Wilk, P. R. Bloemen, T. G. van Leeuwen, M. ter Laan, and M. C. G. Aalders, "Pilot feasibility study of in vivo intraoperative quantitative optical coherence tomography of human brain tissue during glioma resection," J. Biophotonics **12**(10), e201900037 (2019).

22. W. Yuan, C. Kut, W. Liang, and X. Li, "Robust and fast characterization of OCT-based optical attenuation using a novel frequency-domain algorithm for brain cancer detection," Sci. Rep. **7**(1), 44909 (2017).

23. S. R. Bodhireddy, W. D. Lyman, W. K. Rashbaum, and K. M. Weidenheim, "Immunohistochemical detection of myelin basic protein is a sensitive marker of myelination in second trimester human fetal spinal cord," J. Neuropathol. Exp. Neurol **53**(2), 144–149 (1994).

24. M. Hasegawa, S. Houdou, T. Mito, S. Takashima, K. Asanuma, and T. Ohno, "Development of myelination in the human fetal and infant cerebrum: a myelin basic protein immunohistochemical study," Brain Dev **14**(1), 1–6 (1992).

25. F. Varghese, A. B. Bukhari, R. Malhotra, and A. De, "IHC Profiler: an open source plugin for the quantitative evaluation and automated scoring of immunohistochemistry images of human tissue samples," PLoS One **9**(5), e96801 (2014)..

26. K. D. Bergmeister, M. Gröger, M. Aman, A. Willensdorfer, K. Manzano-Szalai, S. Salminger, and O. C. Aszmann, "A rapid automated protocol for muscle fiber population analysis in rat muscle cross sections using myosin heavy chain immunohistochemistry," J. Vis. Exp. **121**, 55441 (2017).

27. K. A. Vermeer, J. Mo, J. J. A. Weda, H. G. Lemij, and J. F. de Boer, "Depth-resolved model-based reconstruction of attenuation coefficients in optical coherence tomography," Biomed. Opt. Express **5**(1), 322–337 (2014).

28. E. V. Gubarkova, A. A. Moiseev, E. B. Kiseleva, D. A. Vorontsov, S. S. Kuznetsov, A. Y. Vorontsov, G. V. Gelikonov, M. A. Sirotkina, and N. D. Gladkova, "Tissue optical properties estimation from cross-polarization OCT data for breast cancer margin assessment," Laser Phys. Lett. **17**(7), 075602 (2020).

29. A. C. Ruifrok and D. A. Johnston, "Quantification of histochemical staining by color deconvolution," Anal. Quant. Cytol. Histol. **23**(4), 291–299 (2011).

30. A. Sen and M. Srivastava, *Regression Analysis: Theory, Methods, and Applications*, 1st ed. (Springer, 1990).

31. A. Altmann, L. Toloşi, O. Sander, and T. Lengauer, "Permutation importance: a corrected feature importance measure," Bioinformatics **26**(10), 1340–1347 (2010).

32. M. A. Hernán, D. Clayton, and N. Keiding, "The Simpson's paradox unraveled," Int. J. Epidemiol. **40**(3), 780–785 (2011).

33. E. B. Kiseleva, K. S. Yashin, A. A. Moiseev, M. A. Sirotkina, L. B. Timofeeva, V. V. Fedoseeva, A. I. Alekseeva, I. A. Medyanik, N. N. Karyakin, L. Ya. Kravets, and N. D. Gladkova, "Cross-Polarization optical coherence tomography in comparative in vivo and ex vivo studies of the optical properties of normal and tumorous brain tissues," Sovrem Tekhnologii Med **9**(4), 177–187 (2017).